Analytica Chimica Acta 1319 (2024) 342959

Contents lists available at ScienceDirect

Analytica Chimica Acta

journal homepage: www.elsevier.com/locate/aca

Exploring novel circulating biomarkers for liver cancer through extracellular vesicle characterization with infrared spectroscopy and plasmonics

R. Di Santo [a,b], F. Verdelli [c], B. Niccolini [a], S. Varca [d], A. del Gaudio [d], F. Di Giacinto [a], M. De Spirito [a,**], M. Pea [e], E. Giovine [e], A. Notargiacomo [e], M. Ortolani [f], A. Di Gaspare [g], A. Baldi [h], F. Pizzolante [d,1], G. Ciasca [a,1,*]

[a] Dipartimento di Neuroscienze, Sezione di Fisica, Università Cattolica del Sacro Cuore & Fondazione Policlinico Universitario "A. Gemelli", IRCCS, Rome, Italy
[b] Dipartimento di Scienze della Vita, della salute e delle Professioni sanitarie, Link Campus University, Rome, Italy
[c] Dutch Institute for Fundamental Energy Research (DIFFER), Eindhoven 5600 HH, The Netherlands
[d] UOC of Gastroenterology, Department of Medical and Surgery Sciences, Fondazione Policlinico Universitario A.Gemelli IRCCS, Università Cattolica del Sacro Cuore, Rome, Italy
[e] Istituto di Fotonica e Nanotecnologie, Consiglio Nazionale delle Ricerche IFN-CNR, Via Del Fosso Del Cavaliere 100, 00133, Rome, Italy
[f] Department of Physics, Sapienza University of Rome, Piazzale Aldo Moro 2, 00185, Rome, Italy
[g] NEST, CNR - Istituto Nanoscienze and Scuola Normale Superiore, Piazza San Silvestro 12, 56127, Pisa, Italy
[h] Department of Physics and Astronomy, Vrije Universiteit Amsterdam, De Boelelaan 1081, 1081 HV Amsterdam, Netherlands

HIGHLIGHTS

- Late diagnosis is a key issue affecting Hepatocellular Carcinoma (HCC) prognosis.
- Patient derived extracellular vesicles (EVs) were analyzed by Mid-IR spectroscopy.
- ATR-FTIR revealed alterations in Amide I-II regions of EVs from HCC patients.
- A plasmonic metasurface was designed to enhance the signal in Amide I-II regions.
- Potential spectral differences between healthy and HCC patients are observed.

GRAPHICAL ABSTRACT

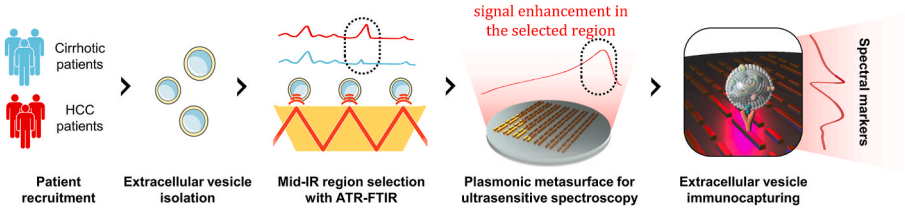

ARTICLE INFO

Handling Editor: Prof Rebecca Lai

ABSTRACT

Background: Hepatocellular carcinoma (HCC) is the most common form of liver cancer, with cirrhosis being a major risk factor. Traditional blood markers like alpha-fetoprotein (AFP) demonstrate limited efficacy in distinguishing between HCC and cirrhosis, underscoring the need for more effective diagnostic methodologies. In this context, extracellular vesicles (EVs) have emerged as promising candidates; however, their practical diagnostic application is restricted by the current lack of label-free methods to accurately profile their molecular content. To address this gap, our study explores the potential of mid-infrared (mid-IR) spectroscopy, both alone and in combination with plasmonic nanostructures, to detect and characterize circulating EVs.

* Corresponding author.
** Corresponding author.
E-mail addresses: marco.despirito@policlinicogemelli.it (M. De Spirito), gabriele.ciasca@unicatt.it (G. Ciasca).
[1] These authors share senior authorship of the work.

https://doi.org/10.1016/j.aca.2024.342959
Received 23 March 2024; Received in revised form 16 June 2024; Accepted 7 July 2024
Available online 8 July 2024

Results: EVs were extracted from HCC and cirrhotic patients. Mid-IR spectroscopy in the Attenuated Total Reflection (ATR) mode was utilized to identify potential signatures for patient classification, highlighting significant changes in the Amide I-II region (1475-1700 cm^{-1}). This signature demonstrated diagnostic performance comparable to AFP and surpassed it when the two markers were combined. Further investigations utilized a plasmonic metasurface suitable for ultrasensitive spectroscopy within this spectral range. This device consists of two sets of parallel rod-shaped gold nanoantennas (NAs); the longer NAs produced an intense near-field amplification in the Amide I-II bands, while the shorter NAs were utilized to provide a sharp reflectivity edge at 1800–2200 cm^{-1} for EV mass-sensing. A clinically relevant subpopulation of EVs was targeted by conjugating NAs with an antibody specific to Epithelial Cell Adhesion Molecule (EpCAM). This methodology enabled the detection of variations in the quantity of EpCAM-presenting EVs and revealed changes in the Amide I-II lineshape.

Significance: The presented results can positively impact the development of novel laboratory methods for the label-free characterization of EVs, based on the combination between mid-IR spectroscopy and plasmonics. Additionally, data obtained by using HCC and cirrhotic subjects as a model system, suggest that this approach could be adapted for monitoring these conditions.

1. Introduction

Hepatocellular carcinoma (HCC) is the most prevalent histological type of liver cancer and ranks as the fourth leading cause of cancer-related deaths worldwide [1]. Nearly 90 % of HCC cases develop in the context of chronic liver disease (CLD). Since cirrhosis represents the strongest risk factor, many patients undergo regular surveillance for early detection. Inconveniently, approximately 50 % of HCC cases are identified incidentally through cross-sectional imaging prompted by unrelated reasons or due to the emergence of severe symptoms associated with advanced-stage HCC. [2]. This diagnostic bottleneck is exacerbated by the limitations of alpha-fetoprotein (AFP), the most widely used circulating HCC marker, which displays poor accuracy with approximately 30 % of HCC patients being AFP-negative [3–6]. Consequently, the development of novel liquid biopsy approaches for HCC diagnosis is highly demanded.

Recent research has focused on exploring circulating extracellular vesicles (EVs) for HCC diagnosis and monitoring [7–9]. EVs are small lipid vesicles secreted by most cell types [10,11]. They are abundant in biofluids and carry molecular cargo reflective of their parent cells, making them promising candidates for circulating cancer biomarkers [11,12]. The current methods for EV analysis, such as mass spectrometry, genomic sequencing, western blotting, or ELISA, are notably time-consuming and/or expensive [13–18]. Moreover, these methods often target only one molecular class at a time or examine a single or a few antigens [19–24], which fail to comprehensively capture the biochemical heterogeneity of EV samples [25].

In this context, Fourier transform infrared (FTIR) spectroscopy, especially in the Attenuated Total Reflectance (ATR) mode, is emerging as a valuable tool [26]. The technique analyses the vibrational modes of molecular bonds upon the absorption of mid-infrared (IR) light in the range of 4000 to 500 cm^{-1} of the electromagnetic spectrum [9,27–29]. Notably, IR spectroscopy offers several advantages compared to other biochemical characterization methods since it provides a comprehensive molecular fingerprint of EVs without requiring sample labeling or complex pre-processing steps that can induce artifacts [30–40].

In addition to downstream biochemical characterization, another factor hindering the spread of EV-based biomarkers in cancer diagnostics is related to purification techniques. Each purification method yields a sample that can be affected differently by the presence of contaminants, which might originate biologically, as is often observed in ultracentrifugation, or being a combination of biological and chemical substances, as frequently encountered in commercial precipitation kits [11,41–44]. Unfortunately, conventional ATR-FTIR faces significant limitations due to the adverse effects caused by contaminants, which act as spectral confounders [11,26]. This effect is further amplified by the fact that all the published studies measured a dry deposit on the ATR crystal, which unavoidably contains a mixture of EVs and confounders of different nature [26]. This poses additional challenges for liquid biopsy applications due to the difficulty of studying a single population of clinically relevant vesicles. For instance, EVs shed by cancer cells in the bloodstream are likely to be a tiny minority compared to those derived from other sources, limiting the specificity of the technique. To address this issue, novel emerging IR technologies, such as Metasurface Enhanced IR spectroscopy (MEIRS), are offering potential solutions [45–53]. MEIRS can be achieved through careful engineering of metallic nanoantennas (NAs) deposited lithographically on an IR-transparent substrate, such as calcium fluoride (CaF_2). By precisely controlling the size, shape, and arrangement of these nanostructures, it becomes possible to attain a remarkable amplification of the electromagnetic field in close proximity to the NA surface and at specific tunable frequencies within the mid-infrared range [54]. Additional technological platforms, including lab-on-chip systems for monitoring and detecting circulating tumor markers, are reviewed in the comprehensive paper by Ratajczak et al. [55].

This study aims to investigate the use of the mid-IR spectral response of circulating EVs as a potential source of novel biomarkers for cancer, with an emphasis on HCC. To achieve this objective, the study included 16 cirrhotic patients without evidence of liver cancer (control group) and 10 HCC patients with underlying cirrhosis. EVs isolated from these patients underwent initial characterization using ATR-FTIR spectroscopy on a dry deposit. This analysis revealed significant spectral differences between the two patient groups, which – upon further validation in future studies – might be instrumental in enhancing the diagnostic performance of AFP.

To address challenges arising from inherent sample impurities, we realized and tested a tailored double-resonant plasmonic metasurface. The metasurface consists of two sets of parallel nanoantennas (NAs) with different lengths (long and short NAs). The long NAs were specifically designed to exhibit a strong plasmonic resonance in the Amide I and II bands of proteins (1600-1700 cm^{-1} and 1475-1600 cm^{-1}, respectively).

Additionally, we exploited the electromagnetic transparent region between the tail of the short and the long NAs' peaks to obtain a reflectivity edge in the 1800–2200 cm^{-1} range, well suited for accurate mass sensing [45]. The metasurface was functionalized with an antibody specific to Epithelial cell adhesion molecule (EpCAM), an antigen found on the EV surface and often overexpressed in various cancer types, including HCC [56–59]. This approach facilitated the quantification of conjugated EVs by leveraging the Surface Plasmon Resonance (SPR) effect exhibited by the NA resonance peak. Simultaneously, owing to the remarkable field enhancement at the NA surface, we measured the specific mid-IR signature of these carefully selected EVs, revealing subtle alterations in the Amide I and II band shapes between the two patient groups.

2. Materials and Methods

2.1. Recruited population

In Table 1, we present the demographic (gender and age), biochemical (hematological indices, liver panel, lipid panel), and clinical characteristics of the recruited population. Specifically, our study group consisted of 16 cirrhotic patients without any indications of liver cancer and 10 HCC patients with cirrhosis as an underlying condition.

The majority of patients were males, with females accounting for only 15 % of the recruited subjects. There was no statistically significant difference in gender distribution between the two groups ($p > 0.9$). However, a notable difference in age was observed ($p = 0.003$, Wilcoxon Rank Sum Test), with a median age of 72 years in cancer patients and 55 years in cirrhotic individuals. This age disparity is a consequence of our study's inclusion criteria, which encompassed HCC patients who had recently developed cancer from an existing condition of cirrhosis. As anticipated, a substantial discrepancy in AFP values was observed, with a median value of 5 units in patients and 2 units in controls ($p = 0.036$).

Furthermore, we noted low Mean Corpuscular Volume (MCV) ($p = 0.061$) and White Blood Cell Count WBC counts ($p = 0.023$) in HCC patients compared to controls.

Table 1
Demographic, biochemical, and clinical attributes of the studied population. Alpha-Fetoprotein (AFP), International Normalized Ratio (INR), Aspartate Aminotransferase (AST), Alanine Aminotransferase (ALT), Platelet Count (PLT), Hemoglobin (Hb), Hematocrit (Ht), Red Blood Cell Count (RBC), Mean Corpuscular Volume (MCV), White Blood Cell Count (WBC), Mean Corpuscular Hemoglobin Concentration (MCHC), Red Cell Distribution Width (RDW), Mean Platelet Volume (MPV), Mean Corpuscular Hemoglobin (MCH), Low-Density Lipoprotein (LDL), High-Density Lipoprotein (HDL), Child-Pugh Score (CHILD), Model for End-Stage Liver Disease (MELD), Model for End-Stage Liver Disease-Na (MELD-NA), Fibrosis-4 Index (FIB-4).

Variable	N	CIRR, N = 16[a]	HCC, N = 10[a]	p-value[b]
Age	26	55 (53, 62)	72 (64, 78)	0.003
Gender	26	M (14), F (2)	M (9), F (1)	>0.9
AFP (ng/mL)	26	2.0 (1.7, 2.4)	4.8 (2.0, 9.6)	0.036
Total Bilirubin (mg/dL)	26	4.7 (1.2, 7.0)	2.2 (1.3, 3.4)	0.3
Direct Bilirubin(mg/dL)	26	2.4 (0.6, 4.3)	1.0 (0.5, 1.5)	0.13
Albumin (g/dL)	26	25.5 (22.0, 28.0)	30.0 (25.9, 33.8)	0.054
Creatinine(mg/dL)	26	0.82 (0.68, 1.63)	0.80 (0.69, 0.85)	0.6
Sodium (mEq/L)	26	137.3 (134.0, 139.0)	138.0 (134.7,140.0)	0.8
INR	26	1.50 (1.20, 1.73)	1.14 (1.11, 1.35)	0.13
AST (U/L)	25	46 (33, 88)	39 (27, 96)	0.7
ALT(U/L)	26	28 (20, 48)	33 (23, 44)	0.8
PLT(U/L)	26	80 (54, 104)	104 (84, 136)	0.3
Hb (g/dL)	26	10.71 (9.62, 12.30)	10.55 (9.71, 12.70)	0.9
Ht (%)	26	31.2 (30.2, 37.8)	31.3 (28.5, 36.4)	0.7
RBC (10^6/μL)	26	3.00 (2.78, 3.96)	3.69 (2.93, 4.03)	0.4
MCV (fL)	26	102 (98, 108)	91 (87, 100)	0.061
WBC (10^3/μL)	26	7.3 (6.5, 8.5)	5.1 (2.7, 6.8)	0.023
MCHC (g/dL)	26	33.10 (32.08, 34.62)	34.30 (33.43, 34.85)	0.12
RDW (%)	26	16.90 (16.20, 18.68)	16.25 (15.57,16.99)	0.2
MPV (fL)	26	9.75 (8.40, 10.45)	9.77 (8.62, 10.83)	0.9
MCH (pg)	26	34.15 (31.62, 36.06)	33.45 (30.42,35.25)	0.4
Total Cholesterol (mg/dL)	17	94 (79, 122)	101 (96, 139)	0.3
LDL (mg/dL)	12	69 (48, 95)	65 (52, 72)	0.8
HDL (mg/dL)	14	11 (7, 14)	26 (14, 36)	0.2
Triglycerides (mg/dL)	14	82 (67, 97)	81 (72, 101)	0.7
CHILD	26	9.00 (8.00, 10.06)	7.50 (5.00, 9.75)	0.2
MELD	25	19 (13, 22)	10 (7, 14)	0.049
MELD-NA	26	20 (14, 25)	11 (7, 18)	0.10
FIB-4	26	5 (3, 11)	1 (0, 10)	0.3

[a] Median (IQR).
[b] Wilcoxon rank sum test; Wilcoxon rank sum exact test.

2.2. Extraction of EV-enriched plasma samples

The patients recruited for this study underwent peripheral blood sampling. Plasma samples were collected and analyzed using infrared spectroscopy. Additionally, aliquots of plasma samples were preserved and used for extracellular vesicle (EV) isolation. Specifically, circulating EVs were isolated using the ExoQuick ULTRA precipitation kit (System Biosciences, Palo Alto, CA, USA) within 24 h of plasma sampling, following the kit manual. The final step of EV isolation involves utilizing columns to obtain samples with higher purity. However, sample purity is a major concern in EV research, as the purification protocol is likely to introduce contaminants from serum or artifacts. To overcome this issue, in this work, we employed EV immunocapturing, as described below, to enable spectral characterization of EVs on the proposed nanostructured device.

2.3. EV characterization

Characterization of EV samples involved transmission electron microscopy (TEM, Fig. S1A) and nanoparticle tracking analysis (NTA, Fig. S1B). For TEM measurements, EV samples were spotted onto Formvar-coated grids and negatively stained with 1 % uranyl acetate. Following staining, the grids were washed three times with distilled water and allowed to air-dry for 1 h. Finally, a Libra 120 microscope (Zeiss, Germany) was used to examine the TEM grids. For NTA measurements, EV samples were diluted with a PBS solution, and the size distribution was evaluated using Nanosight NS300 (NanoSight, UK), registering a final concentration of approximately 10^{10} particles/ml.

2.4. ATR-FTIR measurements

Plasma and EV samples were analyzed using a Bruker ALPHA II compact Fourier Transform Infrared (FTIR) Spectrometer in attenuated total reflection (ATR) mode (ATR-FTIR). Measurements were performed by allowing a volume of 15 μL of plasma/EV sample to dry on the ATR crystal (ZnSe). The IR signal was recorded between 4000 and 600 cm^{-1}, with a resolution of 2 cm^{-1}. Each spectrum consisted of an average of 54 scans. The

background was measured and then subtracted from each spectrum.

2.5. Device fabrication, functionalization, simulation and reflectance measurements

The device design optimization and simulation have been performed with Ansys Lumerical FDTD, as detailed in a previous report [60]. The unit cell, consisting of a gold long rod and two gold short rods on a semi-infinite CaF_2 substrate, has been simulated using periodic boundary conditions. The light is injected bottom to top at normal incidence with both polarization, parallel and orthogonal to the gold rods. The reflection from the array is recorded by a monitor. The overall temperature of the simulation is set at 300 K.

The simulated system has non-uniform meshing with a minimum of 5 nm along the z-direction and 10-nm along the x- and y-direction on the gold structures and 10 nm minimum mesh size everywhere else in the unit cell along all directions. The simulation is set to run until the energy in the system dissipate (indicated in the FDTD software by the autoshutoff threshold of 1e-6) or until it exhausts the time allocated to it (in this case the time allocated is 50000 fs).The simulation time step is set to dt = 0.018 fs with a stability factor of 0.99.

The optimized sensor design was then fabricated using Electron Beam Lithography (EBL) direct writing on a 1-mm thick, optical-grade

CaF_2 substrate (by Crysel), following a previously reported methodology [45]. Briefly, nanostructures were patterned on a 300 nm (900 nm for disk-shaped gold plasmonic antennas) thick Poly(methyl methacrylate) (PMMA) EBL resist layer. To prevent resist and substrate charging during exposure, the PMMA resist layer was coated with a 5 nm thick Cr layer. After exposure, this charge compensation layer was removed, and the resist was developed. The final dipolar antennas were obtained by lift-off technique through the deposition of 10/80 nm Cr/Au metal layers (10/140 nm for disk-shaped gold plasmonic antennas) and subsequent resist stripping in acetone. Sample cleaning was made by sonication in isopropyl alcohol and acetone followed by oxygen plasma treatment.

Initially, the device was immersed overnight in a 10 mM solution of biotinylated polyethylene glycol-thiol (mPEG-Biotin, MW 1000 kD, Nanocs) dissolved in Dulbecco's Phosphate Buffered Saline (DPBS). After PEG binding, the device was washed in DPBS and left for 1 h in a 0.05 mg/mL Neutravidin solution (NeutrAvidin Biotin Binding, ThermoFisher). Finally, a 0.05 mg/mL Anti-EpCAM biotinylated antibody (AMab79079, Abcam) solution was used to further functionalize the device, enabling the capture of EpCAM-expressing EVs.

Before measurements, the patterned CaF_2 window was placed in a 3D-printed wet sample holder, fabricated in Polylactic acid (PLA) through Fusion Deposition Modelling (FDM).

Mid-IR measurements were conducted in reflectance mode at a 25° incidence/reflection angle using unpolarized IR light. Measurements were performed in both liquid and dry environments. The optical geometry was designed so that the incident beam did not directly interact with the water solution but was reflected by the gold nanoantennas, providing a strong back reflection in the far field. Simultaneously, as described in the next section, nanoantennas (NAs) provided an intense near-field enhancement, instrumental for the detection of a small amount of cancer-specific EVs. A small volume of approximately 80 μL of EV sample was used to acquire the spectral profiles of the immunocaptured EVs using the plasmonic metasurface.

2.6. Statistical analysis

Data visualization and statistical analyses were conducted using the software packages R (version 4.2.1), OriginPro 2022, and Stata 18.0. Discrete variables were presented as absolute frequency and/or percentages. Continuous variables underwent normality testing using the Shapiro-Wilk test and visual inspection of the QQ plot (data not shown). Several variables deviated significantly from normality; hence, continuous variables were represented as the median and interquartile range (Q3-Q1). Tabular data were reported using the R package "gtsummary." [61].

For the comparison between the two recruited groups, the Chi-square test or Fisher's exact test was employed for categorical variables, while the Wilcoxon-Mann-Whitney *U* test was used for continuous variables. Statistical significance was set at $p < 0.05$.

The potential diagnostic applicability of the investigated spectral, biochemical, and clinical parameters, both individually and in combination, was evaluated through Receiver Operating Characteristic (ROC) curve analysis. Subsequently, the corresponding Area Under the Curve (AUC) values were computed. The AUC values, along with their confidence intervals, were calculated using the De-Long method and then compared with the value of 0.5, indicating a random classifier. The ROC-AUC analysis was conducted using the "pROC" package in R [62]. The sensitivity, specificity, and threshold at the optimal Youden index were calculated according to the previous paper [63]. A multivariate step-wise logistic regression was performed to select the most informative subset of markers based on the Akaike information criteria (AIC), according to previous report [64].

3. Results

3.1. Preliminary investigation of the spectral response in the Mid-IR range of patient plasma

In the search for possible mid-infrared spectral signatures to discriminate between pathological subjects (HCC) and controls (cirrhosis), an initial exploration was conducted focusing on human plasma (HP) collected from patients. In Fig. 1, we present the average mid-infrared (mid-IR) spectra of HP samples collected from cirrhotic (blue solid line) and HCC (red solid line) patients. Mean spectra are shown together with their corresponding 95 % confidence bands, which are visualized as shaded areas.

For both groups, we have displayed two distinct regions within the mid-IR spectrum: the fingerprint region (1200-1800 cm^{-1}) on the left and the CH stretching band (2800-3000 cm^{-1}) on the right. The process of calculating the average spectra involved separate analyses of these two specified regions. The computation of the means was preceded by a linear baseline correction and followed by area normalization of the spectra. A deeper comparison of the observed spectral features was performed through a box-plot analysis, which involved evaluating the intensities of spectral peaks (Fig. S2). The results of a non-parametric Wilcoxon Mann Whitney *U* test, superimposed on each box plot, confirm the absence of statistically significant differences. These results suggest that the mid-IR response of HP shows limited or no potential efficacy in discriminating between the two pathological states.

3.2. Spectral characterization of EV-enriched samples isolated from patients

EV-enriched samples were extracted from serum samples of cirrhotic and HCC patients. A structural characterization of these samples was performed using Transmission Electron Microscopy (TEM) and Nanoparticle Tracking Analysis (NTA) (Fig. S1). The TEM images display spherical nanoparticles enclosed within double-layered membranes, consistent with the presence and enrichment of EVs in the sample (Fig. S1A). More comprehensive insights into the EV size distribution were derived from NTA measurements, indicating a modal size of approximately 110 nm (Fig. S1B).

In Fig. 2A, we present a comparison of the mid-IR spectral response of EV-enriched samples obtained from cirrhotic patients (depicted by the cyan continuous line) and HCC patients (depicted by the red continuous line). The spectral data were preprocessed as described in the previous section and are presented as the mean along with the corresponding 95 % confidence bands. The figure displays two distinct spectral ranges: the

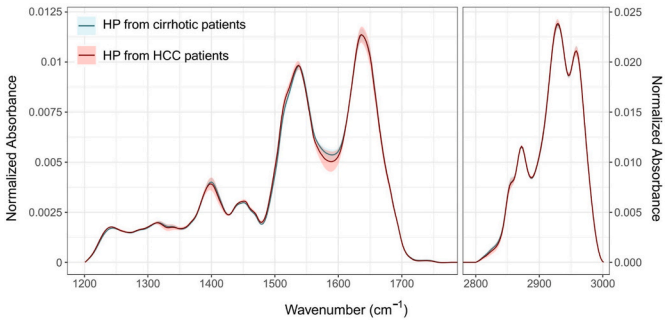

Fig. 1. Comparison of average mid-IR spectra between cirrhotic (blue solid line) and HCC (red solid line) patient samples. Spectra were collected from 15 μl of patient plasma, which was air-dried on the ATR crystal. For each patient, a spectrum consisting of an average of 54 scans was collected. The two distinct regions, the fingerprint region (left, 1200-1800 cm^{-1}) and the CH stretching band of lipids (right), are showcased. Mean spectra are accompanied by 95 % confidence bands (shaded areas). (For interpretation of the references to color in this figure legend, the reader is referred to the Web version of this article.)

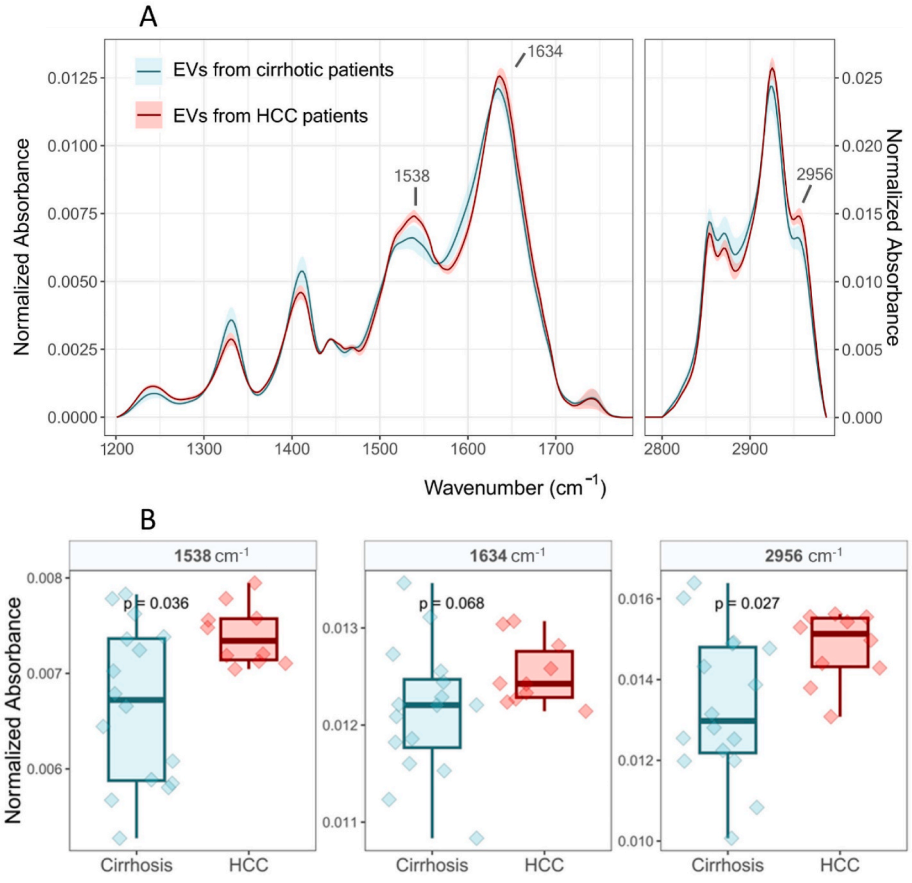

Fig. 2. *Comparison of mid-infrared (mid-IR) spectra between EV-enriched samples from cirrhotic patients without signs of liver cancer (cyan) and HCC patients with underlying cirrhosis (red). The data are represented as means with corresponding confidence bands (A). Spectra were collected from* 15 μl *of each EV sample, which was air-dried on the ATR crystal. For each patient, a spectrum consisting of an average of 54 scans was collected. A box plot analysis illustrates intensity values of mid-IR peaks, indicating statistically significant differences. The statistical comparison of intensities between the two groups was conducted using a non-parametric Wilcoxon rank sum test for independent samples. The results of the test are superimposed on each plot (B). Only spectral features demonstrating statistically significant differences are highlighted in* Fig. 2A *and presented in* Fig. 2B. (For interpretation of the references to color in this figure legend, the reader is referred to the Web version of this article.)

1200-1800 cm^{-1} range on the left and the CH stretching region spanning 2800-3000 cm^{-1} on the right. As performed in section 3.1, these spectral regions are individually presented for each analyzed spectrum in Figs. S3 and S4, respectively.

A qualitative analysis of Fig. 2A suggests the presence of differences between various spectral signatures. Besides variations in peak intensities, confidence bands exhibit greater variability among cirrhotic patients (blue shaded band) compared to cancer patients (red shaded band). To quantitatively capture the observed differences, we compared the spectral peak intensities measured from each subject, as performed in section 3.1. In contrast to plasma, this analysis reveals the presence of statistically significant differences in the spectral intensities at 1538 cm^{-1}, 1634 cm^{-1}, and 2956 cm^{-1}, with the differences at 1634 cm^{-1} being near statistical significance. Fig. 2B displays a box plot analysis of the corresponding intensity values (diamonds) of the peaks. The data are quantitatively compared using a Wilcoxon Mann Whitney *U* test for independent samples, and the p-values are superimposed onto each corresponding plot.

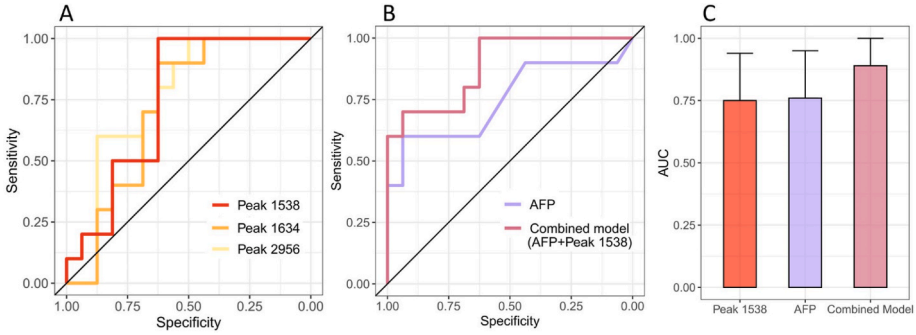

Fig. 3. (A) ROC curves of the statistically significant spectral signatures as highlighted in Fig. 2 (B) Comparison between the full model incorporating AFP and the spectral signature at 1538 cm^{-1}, showcasing ROC curves. (C) Corresponding AUC values (Area Under the Curve) displayed in conjunction with the ROC curves.

3.3. Preliminary evaluation of the spectral marker classification performance and comparison with alpha-fetoprotein

In Fig. 3A, we present an analysis using ROC curves of the significant spectral signatures highlighted in Fig. 2B. Specifically, ROC curves were computed as indicated in the Materials and Methods section by utilizing the peak intensities displayed in Fig. 2 with no additional processing steps. All selected features exhibit areas under the curve that are statistically different from a random classifier (AUC = 0.5). This suggests them as a potential source of HCC biomarkers, which need to be further investigated and validated in dedicated clinical studies with larger patient recruitment. In Fig. S5, further details on the sensitivity, specificity, and threshold at the Youden's point are provided. Subsequently, we conducted a multivariate logistic regression analysis that included all the statistically significant spectral markers along with the corresponding AFP values. A stepwise backward-forward logistic regression was then performed to select the most informative marker combination based on the Akaike Information Criterion. This procedure selected the spectral signature at 1538 cm^{-1} along with AFP levels. In Fig. 3B, we present the ROC curves obtained for the combined model and for AFP alone. The corresponding AUCs along with confidence intervals are displayed in Fig. 3C. Importantly, the combined model displays superior classification performance (AUC = 0.89; 95%CI 0.76–1.00) compared to AFP alone (AUC = 0.75; 95%CI 0.53–0.97).

3.4. Mid-IR spectral response of plasmonic nanoantennas engineered for EV detection via immunocapture and profiling of amide I and II bands

As discussed above, the protein Amide I and II bands of circulating EVs provide a potential source of HCC biomarkers. Unfortunately, this spectral range might be compromised due to the presence of protein impurities from the blood, which co-precipitate with EVs [65,66]. To enhance the sensitivity within this informative spectral range, the separation of a pure EV sample through immunocapture is essential, contributing to eliminating contaminants. Specificity can be further enhanced by targeting EVs shed from cancer cells, which are likely to constitute a minor fraction of EVs released by other sources within the bloodstream, especially in the early stages of the disease [11].

To address this challenge, we have investigated the use of a double-resonant plasmonic sensor, consisting of an array of rod-shaped gold nanoantennas (NAs) with two distinct lengths. For EV sensing, one of the two resonances is centered on the Amide I and II bands, while the second resonance is engineered to exhibit an intense reflection peak at approximately 3000 cm^{-1}, targeting the CH stretching band. A similar design was proposed by Rodrigo et al. [51], focusing on γ-Aminobutyric acid (GABA) vesicles, and later by our group for CD63-mediated EV immunocapture [45].

In Fig. 4A, we examine the IR response (Reflectance %) of the proposed multi-resonant array using a 3D Maxwell FDTD equation solver. The simulation was conducted under both dry conditions (continuous shaded curve) and in a liquid environment (dashed line).

In air, the simulated reflectance spectrum exhibits two prominent resonance peaks, displaying significant overlap with the vibrational signatures of the amide I–II region (1475-1700 cm^{-1}) and the CH stretching bands (2800-3000 cm^{-1}). In a liquid environment, the computed spectrum reveals the expected redshift attributed to the increased index of refraction (RI) of the dielectric half-space. Interestingly, the precise measurement of this redshift can be employed for real-time mass sensing, as will be described in the following [45]. Importantly for our purposes, in both conditions, a nearly transparent electromagnetic region is observable within the 1800–2200 cm^{-1} range (grey shaded area), where no absorption of biological molecules is expected. This electromagnetic transparent region displays an interesting behavior in the two environmental conditions. Upon changing the medium, the remaining portions of the spectrum undergo a redshift, accompanied by a remarkable change in line shapes. Conversely, the mentioned dip in reflectance undergoes an almost pure redshift without notable alterations in spectral shape. This rigid translation makes this spectral feature an ideal candidate for quantitatively measuring the redshift of the antenna associated with the local RI change stemming

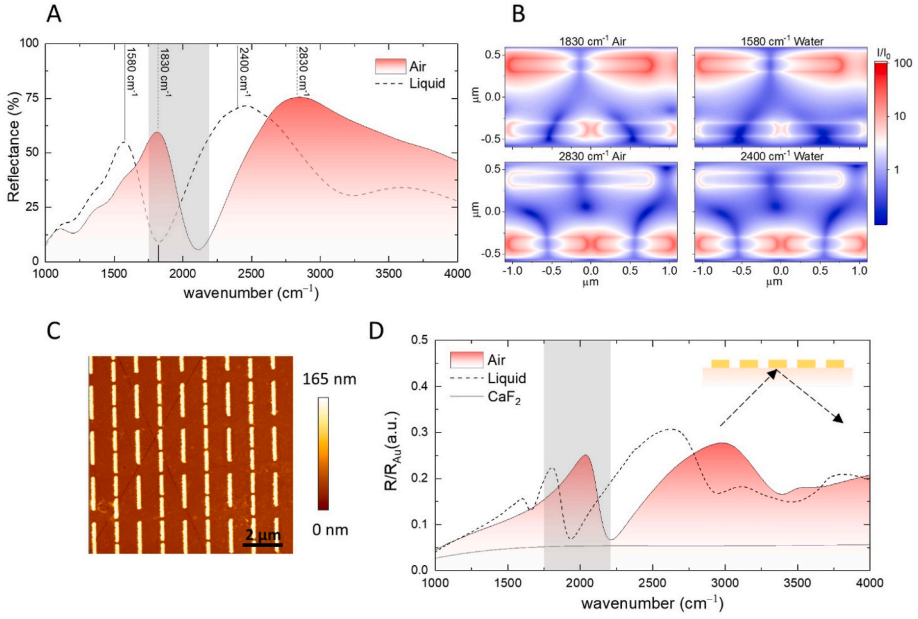

Fig. 4. Electromagnetic design of the multi-resonant metasurface platform consisting of NAs of two different lengths, namely short nanoantennas (L_1 = 1 μm) and long nanoantennas (L_2 = 1.826 μm). The reflectance spectrum (R%) is simulated using Finite Difference Time Domain (FDTD) in both air (solid black line with shaded area) and liquid (dashed curve). The Savitzky-Golay (SG) smoothing technique has been employed in the data visualization. Spatially resolved near-field enhancement (I/I_0) maps in air and in a liquid environment, shown at two specific wavenumbers corresponding to vertical lines in panel A (1830 and 2830 cm^{-1} in air, and 1580 and 2400 cm^{-1} in liquid). Representative AFM topography of a fabricated plasmonic array (C). Spectral response of the nanoantennas in dry (solid black line with shaded area) and liquid (dashed curve, with nanoantennas covered by 80 μl of water) conditions (D). The nanoantenna response is shown alongside that of a CaF_2 substrate (C, grey continuous curve).

from EV immunocapture.

Fig. 4B complement this analysis with FDTD simulations of the spatially-resolved near-field enhancement (I/I_0) on the NA surface in air and liquid environments, computed at selected wavenumbers corresponding to the peak frequencies in Fig. 4A (vertical lines). One can observe that NAs with different lengths are excited at their corresponding resonance frequencies, exhibiting a strong near-field enhancement (bright red color). Specifically, the long antennas resonate at approximately 1830/1580 cm^{-1} in air/water, while the short antennas resonate at approximately 2830/2400 cm^{-1} in air/water, aligning with the two intense resonance peaks observed in the computed reflectance spectrum (Fig. 4A, vertical lines).

Fig. 4C shows a representative AFM topography of NAs realized according to the previously discussed design. This patterned surface was arranged in a specifically designed 3D printed sample holder, and the reflectance spectra were acquired at a 25° angle of incidence/reflectance, in both dry and liquid environments (Fig. 4D). Consistent with prior studies [45,51], the plasmonic chip is illuminated from the dry side of the CaF_2 substrate, while the NAs are immersed in the target solution (Fig. 4D, Inset). The spectra are represented alongside the spectrum of the CaF_2 optical window (Fig. 4D, continuous grey line).

Reflectance values are normalized to the reflectance of a flat 100 nm gold film evaporated on a CaF_2 optical window. A qualitative examination of the spectra reveals a close agreement with the previously discussed electromagnetic design (Fig. 4A). Specifically: (i) two distinct antenna resonances are observed in air, aligning significantly with the vibrational characteristics of the amide I–II region and the CH stretching bands; (ii) the expected redshift is observed by changing the medium from air to PBS; (iii) the previously mentioned nearly transparent electromagnetic region within the 1800–2200 cm^{-1} range is also identified. A slight distortion in the observed reflectance compared to the simulation in Fig. 4A spectra is likely attributed to the change in incident angle between the simulation (normal incidence) and measurements (25°). Additionally, the broad IR absorption bands of water (centered at 1650 and 3300 cm^{-1}) unavoidably overlap with the reflectance spectra acquired in a liquid environment. Despite the presence of these absorption bands, the measured reflectance confirms the existence of a significant multiresonant near-field enhancement within the spectral region of interest.

3.5. Real-time in-situ monitoring of EV deposition on metasurface via cancer-related antigen-mediated immunocapture

In this section, we assess the real-time, liquid-phase immunocapture of patients' EVs expressing cancer-related antigens. To achieve this, NAs were conjugated with an antibody specific for EpCAM, an antigen present on the EV surface and overexpressed in many cancer types [67].

In contrast to the shift induced by the transition from an air to a liquid phase (Fig. 4A and D), which is associated with a significant alteration in the refractive index, the redshift resulting from the formation of an EV monolayer seems not to be directly measurable through the unaltered antenna response. Instead, it becomes distinctly discernible through the computation of the time-varying differential signal, defined as $D(t) = R(t) - R_0$, where $R(t)$ and R_0 represent the reflectance of the NAs at time t and time 0, respectively.

In Fig. 5A, we show a map of the time-dependent behavior of the above-mentioned signal. A qualitative analysis of this map reveals remarkable alterations within the electromagnetic transparency region of the antennas, situated around approximately 1950 cm^{-1}. In Fig. 5B, we showcase the sensor response at specific time points (vertical lines in Fig. 5A), starting from 0 (bold green flat curve) at intervals of 2.5 min (green curves). Furthermore, we highlight the final data point of the kinetics at approximately 26.7 min (bold green curve).

Overall, Fig. 5B displays a negative peak in the difference signal around 1950 cm^{-1}, which intensifies over time. In Fig. 5C, we demonstrate that this behavior is consistent with an antenna redshift that can be used for refractive index/mass sensing. To achieve this, we took the antenna spectrum at time 0, before EV immunocapture has occurred and we interpolated it linearly with an increment of 0.1 cm^{-1}. The interpolated curve was then manipulated to induce a controlled redshift by appropriately adjusting the position of the intensity values relative to wavenumbers. We computed a total of 9 different curves, each with a redshift ranging from 0 to 4 cm^{-1}. Interestingly, we observed the same qualitative trend between the curves recorded during the kinetic immunocapture of EVs and the simulated spectrum. This unambiguously demonstrates that the time-dependent changes reported in Fig. 5A and B are a result of an antenna redshift, which is associated with the progressive immunocapture of the EVs on the NAs' surface. By comparing the values in Fig. 5B and C, it is possible to estimate a redshift of approximately 1 cm^{-1} attributed to the immunocapture of the vesicles.

It is important to emphasize that this slight shift would be challenging to observe from the antenna spectrum without manipulations, such as calculating the difference signal D(t). Additionally, it would be

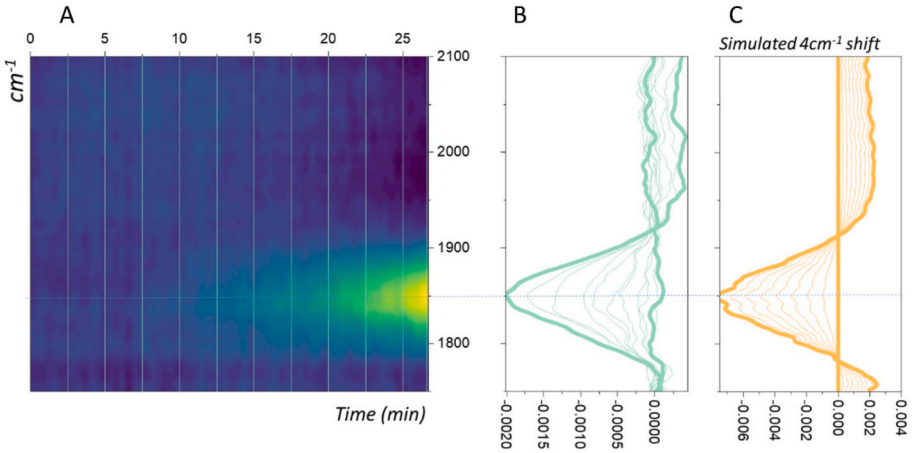

Fig. 5. Color map illustrating the time-dependent changes of the Antenna difference signal, denoted as $D(t) = R(t) - R(0)$. Here, $R(t)$ and $R(0)$ respectively represent the reflectance of the NA at time t and time 0. The signal was acquired during the immunocapturing of the EVs on the nanoantennas over time (~ 80 μl of EV sample) (A). The section of the figure showcases specific time points (B), as indicated by the vertical lines in Fig. 5A. Additionally, the figure includes 9 simulations of antenna redshift ranging from 0 to 4 cm^{-1}, with an incremental step of 0.5 cm^{-1} (C). A comparison between panels B and C enables the estimation of an experimental redshift of approximately 1 cm^{-1}. (For interpretation of the references to color in this figure legend, the reader is referred to the Web version of this article.)

difficult to detect without the use of the carefully engineered dip in the reflectance, as illustrated in Fig. 4 and observed in Fig. 5. This point is further discussed in Fig. S6, where we present the results of a different plasmonic array with higher reflectance but in the absence of the mentioned peak. Despite conducting measurements on the same EV sample and employing the same antenna functionalization, Fig. S6, in contrast to Fig. 5, does not exhibit useable signatures for refractive index (RI)/mass sensing.

3.6. Detection of specific amide I and II signatures of EpCAM-Expressing EVs derived from patients

In Fig. 6, we analyze the spectral response of our NAs subsequent to the immunocapture of EVs obtained from patients diagnosed with cirrhosis and HCC. To achieve this, two distinct sample pools were derived from the two groups of patients. As previously discussed, the EVs were immobilized in close proximity to the NAs' surface through immunocapture, specifically targeting EpCAM on the EV surface. Following the EV immunocapture step, which was monitored as illustrated in Fig. 5, the metasurface was immersed in deionized water and then dried in a nitrogen stream. This process aimed to terminate the immunocapture kinetics while concurrently eliminating nonspecific binding of analytes/contaminants. Subsequently, the reflection of the functionalized metasurface was measured in a dry environment. In Fig. 6A, we report an enlarged detail of the metasurface spectrum in the 1000 to 2200 cm^{-1} range. Three conditions are shown: the surface without immunocapture functionalization (black line), the surface functionalized for immunocapture (gold line), and the surfaces with immobilized EVs on them (red dashed line for HCC patients and green dashed line for cirrhotic ones). A redshift of approximately 20 cm^{-1} can be readily observed by comparing the metasurface spectra before and after EpCAM functionalization. An additional redshift of around 12 cm^{-1} is evident when comparing the spectra of the EpCAM-functionalized metasurface before and after EV immunocapture. The more substantial redshift observed in Fig. 6A compared to measurements in liquid is not unexpected, as the local increase in the index of refraction due to immunocapture is greater in air than in liquid.

Notably, the antenna response distinctly reveals the presence of specific spectral signatures corresponding to the Amide I and II bands in the EpCAM-functionalized sample, as well as in the EV-conjugated ones (black arrows). A reduced intensity of this signature is observed in EpCAM-only compared to EVs. A more meticulous analysis of the spectra from patients reveals a subtle yet perceptible increase in the intensity of the Amide I and II peaks in HCC samples compared to cirrhosis. From these measurements, we derived the Absorbance A_1 of the conjugated EpCAM molecules using the equation $A_1 = -\ln(R_{EpCAM}/R_0)$. In this equation, R_{EpCAM} represents the reflectance of the metasurface conjugated with Neutravidin and EpCAM molecules, while R_0 is the initial reflectance of the pegylated metasurface, adjusted for the appropriate compensation for redshift. The EV signal was extracted using a similar procedure. After applying the necessary redshift compensation, we calculated the cumulative signal resulting from EVs, EpCAM, and Neutravidin molecules, employing the equation $A_2 = -\ln(R_{EV}/R_0)$, where R_{EV} stands for the reflectance of the EV-conjugated metasurface. Ultimately, to isolate the signal exclusively from EVs, we subtracted the two absorbance values: $A_{EV} = A_2 - A_1$.

In Fig. 6B, we compare the absorbance spectra in the wavenumber region of 1500–1800 cm^{-1} for the pool of patients diagnosed with HCC (above) and the controls diagnosed with hepatic cirrhosis. The amide I and II bands are observed to be centered at approximately 1660 cm^{-1} and 1550 cm^{-1} for both types of samples, suggesting a different secondary structure content compared to Fig. 2, wherein peak values were around 1634 cm^{-1} and 1538 cm^{-1}, respectively. This conformational change is consistent with a higher contribution of contaminants in Fig. 2. This hypothesis is reinforced by the fact that the amide I peak in this latter figure is closer to 1640 cm^{-1}, a value characteristic of albumin, which is the most commonly occurring protein in the blood, thus acting as a potential spectral confounder [68].

A more in-depth analysis of Fig. 6 reveals an additional peak at approximately 1730 cm^{-1} that overlaps with the Amide I band, which could be attributed to the lipid ester peak. Importantly, with respect to Fig. 2, this peak carries a higher relative weight compared to the amide I peak. This proportional increase in intensity is consistent with the fact that our measurement involves a sample exclusively composed of EVs, thereby exhibiting a higher lipid percentage than a sample that might contain protein contaminants. Additionally, these lipids are positioned near the antenna surface, where electromagnetic field amplification is at its maximum. Ultimately, by integrating the signatures in the analyzed spectral range, we obtained a total area of approximately 4.1 cm^{-1}*(a.u.) for HCC and 3.26 cm^{-1}*(a.u.) for cirrhotic subjects. This area enhancement in HCC subjects could be due to an overall increase in EV protein content or to affinity reasons associated with heightened EpCAM expression. Although our sensor is incapable of distinguishing between these two contributions, we believe the latter is more likely, as EpCAM overexpression is expected in EVs derived from many cancer types.

4. Discussions and conclusions

The diagnosis of HCC currently involves a combination of diverse methods, encompassing the analysis of circulating markers, medical

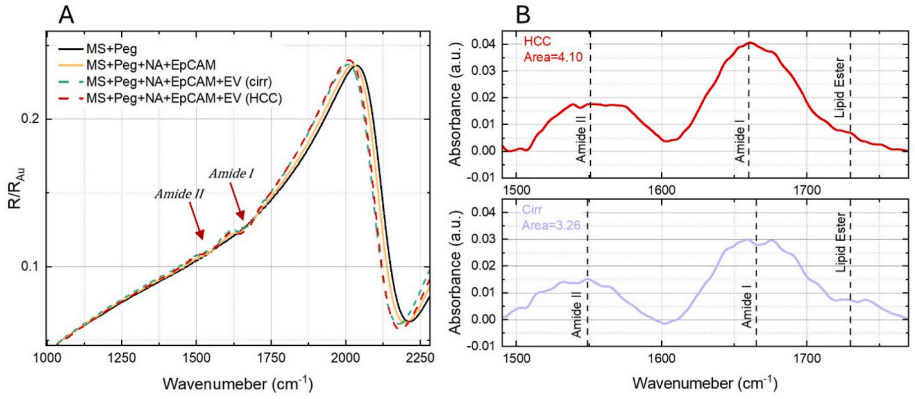

Fig. 6. Spectral response of our NAs following the EV immunocapture. (A) An expanded view of the metasurface (MS in the legend) spectrum in the 1000 to 2200 cm^{-1} range is presented, displaying three conditions - the unfunctionalized metasurface (black line), the metasurface prepared for immunocapture (gold line), and the metasurface post-EV immunocapture (with red dashed line representing HCC patients and green dashed line for cirrhotic patients). (B) spectral response in the wavenumber region of 1500–1800 cm^{-1} for the pool of HCC (above) and cirrhotic patients. (For interpretation of the references to color in this figure legend, the reader is referred to the Web version of this article.)

imaging techniques, and histopathological biopsies [1–4]. However, these methods possess limitations that can impact patient prognosis. Specifically, medical imaging demonstrates a restricted capability to detect small tumors, leading to a large number of false negatives and reduced sensitivity. Histopathology also encounters several challenges due to its invasive nature and occurrence of false negatives [69–73]. Circulating biomarkers are widely employed for assessing liver damage, primarily relying on liver enzyme profiles such as aspartate aminotransferase (AST) and alanine aminotransferase (ALT) [56,58,74–77]. However, these enzymes lack specificity for liver diseases. Traditional tumor markers like AFP and lens culinaris-agglutinin-reactive fraction of AFP (AFP-L3) are also prone to interference from other liver conditions such as cirrhosis, leading to their limited sensitivity and specificity for HCC [3,4,6,56]. Nonetheless, combining multiple parameters has shown promise in enhancing diagnostic performance [4,73,78–80]. Consequently, the search for novel, specific markers or marker combination for patients with liver diseases takes on paramount significance [73,81].

In this context, a large body of evidence highlighted the potential of studying the molecular cargo carried by circulating EVs [9,56,57,82,83]. Concerning liver pathologies, increased levels of circulating EVs have been found in alcoholic liver disease, non-alcoholic steatohepatitis (NASH), viral hepatitis, drug-induced liver injury and hepatocellular carcinoma [83]. As for HCC, EVs do indeed play a significant role in disease progression, influencing numerous biological pathways. This includes the modulation of immune and endothelial cell functions, promoting immune evasion, and angiogenesis [71,84,85]. The comprehensive review by Kalluri & McAndrews illustrates how EVs mediate interactions between Kupffer cells, hepatocytes, and stellate cells, influencing the onset of NASH and liver cancer through mechanisms involving miR-690, IRE1A, and proinflammatory signalling [86]. Additionally, EVs influence the Epithelial to Mesenchymal Transition [87], and activates the inflammatory microenvironment to enhance cancer cell invasiveness, converting fibroblasts and macrophages into cancer-associated fibroblasts (CAFs) and tumor-associated macrophages (TAMs) [71,88,89].

In this paper, we investigated the applicability of a novel approach for the detection and molecular characterization of circulating EVs. HCC and cirrhotic patients were recruited as a model system, and the IR signatures of circulating EVs were compared. For this purpose, we use conventional ATR-FTIR spectroscopy in the mid-IR range, as well as specifically designed resonant plasmonic nanostructures for surface-enhanced spectroscopy both in liquid and dry phase.

Interestingly, while no significant differences were highlighted in the spectral response of plasma extracted from the two groups, the ATR-FTIR spectra of EVs show remarkable alteration in the peak intensities at 1538 cm^{-1} (assigned to amide II of proteins) and at 2956 cm^{-1} (assigned to CH stretching of lipids). Changes at 1538 cm^{-1} can be associated either with an alteration of the protein conformational state or to a change in the protein types and concentration within EVs. Interestingly, our results are in line with other findings showing alterations in EV proteins according to the environment and state of liver cells [83,90–100]. While IR spectroscopy may not be capable of detecting alterations in individual proteins, it can detect changes in the overall protein content by analyzing the shape and intensity of the amide I and II bands. Importantly, these changes can serve as effective markers of pathology. In Fig. 3, indeed, we demonstrate that the intensity at 1538 cm^{-1} shows a considerable ability to discriminate between HCC patients and cirrhotic patients, no less than AFP in the same group of subjects. Most notably, the combination of AFP with this spectral marker leads to a remarkable AUC of 0.89 (95 % CI 0.76–1.00).

Fig. 3 selects the intensity of the Amide II band instead of the more commonly used Amide I as an HCC marker. This choice was based on the results of a stepwise logistic regression that identified this peak as the most informative [101]. Notably, this purely statistical rationale finds some interesting parallels in the literature, such as the ground-breaking work of Kim et al. [102]. The authors employed a synergistic approach, combining AFM microscopy and IR spectroscopy (AFM-IR). Through this methodology, they successfully identified areas within EV samples exhibiting elevated protein content, primarily attributed to contaminants from the extraction medium. Notably, these regions were consistently associated with a prominent amide I peak, in contrast with the predominance of the amide II band exhibited in region with EVs alone. Therefore, we can hypothesize that the statistical selection of the amide II band may be correlated with a reduced detrimental effect of contaminants from blood on this peak. This hypothesis is further strengthened by the findings reported in Fig. 1, which shows no significant spectral differences correlated with plasma proteins.

Over the past two decades, the field of IR spectroscopy has witnessed significant advancements driven by innovative technologies, encompassing tip-enhanced and surface-enhanced spectroscopies [26]. These technologies hold the promise to establish IR spectroscopy as a central player in the EV science, being well-suited to address key limitations and challenges in the field. Notably, one of the primary challenges revolves around EV purification techniques, each impacting samples differently due to the presence of contaminants [11]. To address this complex issue, we utilized a specifically designed plasmonic metasurface combined with immunocapture mediated by EpCAM, an antigen commonly overexpressed in many cancer types. This approach enabled us to selectively target a clinically relevant sub-population of EVs and analyze the corresponding spectral response. While EpCAM immunocapture does not guarantee that all detected EVs originate from cancer cells, it increases the likelihood of isolating a population enriched with cancer-derived vesicles. Moreover, the near-field enhancement provided by the metasurface helps address the challenges of limited sample availability, particularly critical when analyzing EV subpopulations. This combined method effectively eliminates protein contaminants from the plasma, as it measures only those EVs that are in close proximity to the nanostructures. As such, this technique could represent a substantial advancement over traditional ATR-FTIR studies, which, to our knowledge, have previously relied solely on solid residues when investigating EVs. [26].

By leveraging the tunable nature of plasmonic resonance, we engineered a NA array exhibiting a strong resonance in the amide I and II range, both in air and liquid environments. Notably, when comparing the spectral responses in the 1480-1750 cm^{-1} range between ATR-FTIR and our plasmonic antennas, significant differences in the amide I and II bands emerged, providing clear evidence that we are observing distinct samples. Interestingly, the spectra measured by the antennas show a pronounced lipid ester peak (1730 cm^{-1}), supporting the claim that we are not observing a predominantly proteinaceous sample but rather one with a substantial lipid component.

In this study, some limitations could be identified that might negatively impact the translational process of the proposed technology in diagnostic practice. A significant challenge may arise from the use of EBL for the fabrication of plasmonic nanostructures. While EBL offers precision, it also involves high costs and limited scalability. To directly address these challenges, alternative fabrication techniques should be explored, which promise greater potential for mass production at lower costs. These alternatives might include advanced methods such as Extreme Ultraviolet (EUV) lithography, capable of achieving ridges of critical dimensions below 70 nm [103], a resolution sufficient to replicate our nanostructures. A further scalability boost is suggested in the excellent review by John-Herpin, which discusses the potential impact of doped semiconductors and complementary metal-oxide-semiconductor (CMOS)-compatible metals for scalable mass production of mid-IR sensors [104].

Another limitation relates to the potential lack of specificity of the amide I and II signals. These bands are ubiquitous across biological samples and can be influenced by a broad range of clinical conditions, making their use in cancer diagnostics challenging. However, it is important to emphasize that this general lack of specificity is not uncommon for circulating biomarkers. In actual biomedical scenarios,

single markers rarely achieve high specificity. More often, clinical scores are developed using a combination of multiple markers, each with modest specificity, to enhance diagnostic accuracy. This approach is widely applied in the diagnosis and monitoring of CLDs, which rely on various scoring systems. These include APRI, which incorporates platelet count; FIB-4, which includes platelet count and age; FibroTest, featuring apolipoprotein A1; FORN, which includes platelet count, age, and cholesterol level; and Fibrometer, which involves glucose, ferritin, platelet count, and body mass index [105,106]. Similar to spectral signatures, these markers may lack specificity when used alone, but they achieve greater clinical significance when thoughtfully combined with other parameters. A example of this combination is demonstrated in Fig. 4. Therefore, integrating our IR-plasmonic signatures into suitable multi-marker panels represents a mandatory future research direction for the proposed technology.

To address the specificity issue, another viable solution involves achieving an even higher signal-to-noise ratio capable of distinguishing subtle disease-specific band shape modifications. To this end, considering alternative designs to the dipolar antenna could significantly enhance detection capabilities. These designs include aperture and narrow-gap antenna arrays [104]; however, the use of these designs may introduce additional challenges related to the precise delivery of the analyte to the antenna load.

Considering future research directions, it is instructive to examine the recent work by Shin et al. [107], which employed surface-enhanced spectroscopy techniques, albeit applied to Raman rather than IR spectroscopy, and paired with advanced machine learning classifiers. This approach successfully distinguished between seven clinical conditions (healthy donors and six different types of cancers) based on spectral signatures, achieving remarkable AUC values. Beyond the use of machine learning methods, the substantial patient enrollment—several hundreds of patients—was a critical factor in achieving such high diagnostic accuracy. This robust sample size is a necessary next step to stimulate the translation of the proposed technique into diagnostics, underscoring the importance of extensive clinical validation in enhancing the reliability and applicability of the proposed method.

In summary, we propose a methodological approach for the characterization of circulating EVs based on mid-IR spectroscopy, both alone and in combination with resonant plasmonic sensors. Using the progression from cirrhosis to HCC as a model system, we identified possible clinically relevant differences in the EV spectral response. These signatures might serve as a future source of HCC biomarkers upon validation in a dedicated clinical study with robust patient recruitment. Notably, our preliminary results on diagnostic performance already demonstrate capabilities comparable to currently utilized circulating markers, such as AFP, and confirm the potential to synergistically combine these features with established markers to enhance diagnostic accuracy. To effectively translate these spectral markers into clinical practice, it is crucial to develop a technique capable of acquiring information from circulating vesicles released by cancerous cells, which likely constitute a minority portion of the overall vesicle population. Additionally, the technique should address the challenge of eliminating spectral contaminants within EV samples.

In this regard, our study proposes using a plasmonic platform made of rod-shaped gold nanoantennas operating in the mid-infrared range, both in liquid and dry environments. Through appropriate functionalization, this platform selectively captures clinically relevant vesicles shed by cancer cells while simultaneously eliminating contaminants.

Importantly, the article introduces a method to fully exploit the tunability of these nanostructures. This method involves an initial investigation of the EV sample using ATR-FTIR on a solid deposit on the ATR crystal, followed by the identification, through biostatistical methods, of the most promising spectral regions to define a circulating spectral biomarker. Through a rigorous electromagnetic design and accurate fabrication process, the nanoantenna array can then be tailored to exhibit the maximum field enhancement at the selected frequencies, thereby maximizing the technique's specificity across different clinical settings.

CRediT authorship contribution statement

R. Di Santo: Writing – review & editing, Writing – original draft, Visualization, Methodology, Investigation, Formal analysis, Data curation, Conceptualization. **F. Verdelli:** Visualization, Software, Investigation, Data curation. **B. Niccolini:** Methodology, Investigation. **S. Varca:** Resources. **A. del Gaudio:** Resources. **F. Di Giacinto:** Software, Data curation. **M. De Spirito:** Writing – review & editing, Supervision. **M. Pea:** Writing – review & editing, Resources, Investigation. **E. Giovine:** Supervision, Conceptualization. **A. Notargiacomo:** Writing – review & editing, Resources, Investigation. **M. Ortolani:** Supervision, Conceptualization. **A. Di Gaspare:** Resources, Investigation. **A. Baldi:** Supervision, Conceptualization. **F. Pizzolante:** Writing – review & editing, Supervision, Resources, Project administration. **G. Ciasca:** Writing – review & editing, Writing – original draft, Visualization, Supervision, Project administration, Methodology, Funding acquisition, Conceptualization.

Declaration of competing interest

The authors declare that they have no known competing financial interests or personal relationships that could have appeared to influence the work reported in this paper.

Data availability

Data will be made available on request.

Acknoledgements and Funding

Riccardo Di Santo was supported by Fondazione Umberto Veronesi, which is gratefully acknowledged. This research was funded by the Italian Ministry of Health, "Progetto Giovani Ricercatori 2015-2016", grant number GR-2016-02363310. Università Cattolica del Sacro Cuore is also gratefully acknowledged for supporting the research and the gold open access.

Appendix A. Supplementary data

Supplementary data to this article can be found online at https://doi.org/10.1016/j.aca.2024.342959.

References

[1] J.D. Yang, P. Hainaut, G.J. Gores, A. Amadou, A. Plymoth, L.R. Roberts, Nat. Rev. Gastroenterol. Hepatol. 16 (2019) 589–604.
[2] J.M. Llovet, R.K. Kelley, A. Villanueva, A.G. Singal, E. Pikarsky, S. Roayaie, R. Lencioni, K. Koike, J. Zucman-Rossi, R.S. Finn, Nat. Rev. Dis. Prim. 7 (2021) 1–28.
[3] P. Luo, S. Wu, Y. Yu, X. Ming, S. Li, X. Zuo, J. Tu, Pathol. Oncol. Res. 26 (2020) 599–603.
[4] U. Basile, L. Miele, C. Napodano, G. Ciasca, F. Gulli, K. Pocino, N. De Matthaeis, A. Liguori, A. De Magistris, G. Marrone, M. Biolato, M. Marino, F. Di Giacinto, A. Gasbarrini, A. Grieco, G.L. Rapaccini, Eur. Rev. Med. Pharmacol. Sci. 24 (2020) 12675–12685.
[5] H. Park, J.Y. Park, BioMed Res. Int. 2013 (2013).
[6] J. Zhang, G. Chen, P. Zhang, J. Zhang, X. Li, D. Gan, X. Cao, M. Han, H. Du, Y. Ye, PLoS One 15 (2020) e0228857.
[7] R. Chen, X. Xu, Y. Tao, Z. Qian, Y. Yu, Cell Commun. Signal. 17 (2019) 1–11.
[8] Y.-T. Lee, B. V Tran, J.J. Wang, I.Y. Liang, S. You, Y. Zhu, V.G. Agopian, H.-R. Tseng, J.D. Yang, Cancers 13 (2021) 3076.
[9] R. Di Santo, M. Vaccaro, S. Romanò, F. Di Giacinto, M. Papi, G.L. Rapaccini, M. De Spirito, L. Miele, U. Basile, G. Ciasca, J. Personalized Med. 12 (2022) 949.
[10] M. Tkach, C. Théry, Cell 164 (2016) 1226–1232.
[11] R. Di Santo, S. Romanò, A. Mazzini, S. Jovanović, G. Nocca, G. Campi, M. Papi, M. De Spirito, F. Di Giacinto, G. Ciasca, Nanomaterials 11 (2021) 1476.
[12] T. Katsuda, N. Kosaka, T. Ochiya, Proteomics 14 (2014) 412–425.
[13] T.A. Hartjes, S. Mytnyk, G.W. Jenster, V. van Steijn, M.E. van Royen, Bioengineering 6 (2019) 7.

[14] A. Hendrix, L. Lippens, C. Pinheiro, C. Théry, L. Martin-Jaular, J. Lötvall, C. Lässer, A.F. Hill, K.W. Witwer, Nat. Rev. Methods Prim. 3 (2023) 56.
[15] B. Vestad, A. Llorente, A. Neurauter, S. Phuyal, B. Kierulf, P. Kierulf, T. Skotland, K. Sandvig, K.B.F. Haug, R. Øvstebø, J. Extracell. Vesicles 6 (2017) 1344087.
[16] C. Gardiner, Y.J. Ferreira, R.A. Dragovic, C.W.G. Redman, I.L. Sargent, J. Extracell. Vesicles 2 (2013) 19671.
[17] R. Linares, S. Tan, C. Gounou, A.R. Brisson, Exosomes Microvesicles Methods Protoc, 2017, pp. 43–54.
[18] L.G. Rikkert, R. Nieuwland, L. Terstappen, F.A.W. Coumans, J. Extracell. Vesicles 8 (2019) 1555419.
[19] G. Pocsfalvi, C. Stanly, A. Vilasi, I. Fiume, G. Capasso, L. Turiák, E.I. Buzas, K. Vékey, Mass Spectrom. Rev. 35 (2016) 3–21.
[20] D. Choi, D. Kim, Y. Kim, Y.S. Gho, Mass Spectrom. Rev. 34 (2015) 474–490.
[21] K.M. Kim, K. Abdelmohsen, M. Mustapic, D. Kapogiannis, M. Gorospe, Wiley Interdiscip. Rev. RNA 8 (2017) e1413.
[22] J. Elzanowska, C. Semira, B. Costa-Silva, Mol. Oncol. 15 (2021) 1701–1714.
[23] J. Ko, Y. Wang, K. Sheng, D.A. Weitz, R. Weissleder, ACS Nano 15 (2021) 5631–5638.
[24] E.J.K. Kowal, D. Ter-Ovanesyan, A. Regev, G.M. Church, Extracell. Vesicles Methods Protoc (2017) 143–152.
[25] E. Willms, C. Cabañas, I. Mäger, M.J.A. Wood, P. Vader, Front. Immunol. 9 (2018) 738.
[26] R. Di Santo, B. Niccolini, S. Romanò, M. Vaccaro, F. Di Giacinto, M. De Spirito, G. Ciasca, Spectrochim. Acta Part A Mol. Biomol. Spectrosc. (2023) 123346.
[27] L. Paolini, S. Federici, G. Consoli, D. Arceri, A. Radeghieri, I. Alessandri, P. Bergese, J. Extracell. Vesicles 9 (2020) 1741174.
[28] V. Swaminathan, K. Mythreye, E. Tim O'Brien, A. Berchuck, G.C. Blobe, R. Superfine, Cancer Res. 71 (2011) 5075–5080.
[29] O. Faix, in: Methods Lignin Chem, Springer, 1992, pp. 83–109.
[30] J.K. Victoria Ramos-Garcia, Isabel Ten-Doménech, Alba Moreno-Giménez, Marìa Gormaz, Anna Parra-Llorca, Alex P. Shephard, Pilar Sepùlveda, David Pérez-Guaita, Màximo Vento, Bernhard Lendl, Guillermo Quintàs, V. Ramos-Garcia, I. Ten-Doménech, A. Moreno-Giménez, M. Gormaz, A. Parra-Llorca, A.P. Shephard, P. Sepúlveda, D. Pérez-Guaita, M. Vento, B. Lendl, Chemometr. Intell. Lab. Syst. 217 (2021) 104401.
[31] L. Pascucci, V. Coccè, A. Bonomi, D. Ami, P. Ceccarelli, E. Ciusani, L. Viganò, A. Locatelli, F. Sisto, S.M. Doglia, E. Parati, M.E. Bernardo, M. Muraca, G. Alessandri, G. Bondiolotti, A. Pessina, J. Contr. Release 192 (2014) 262–270.
[32] T. Bebesi, D. Kitka, A. Gaál, I.C. Szigyártó, R. Deák, T. Beke-Somfai, K. Koprivanacz, T. Juhász, A. Bóta, Z. Varga, Sci. Rep. 12 (2022) 977.
[33] M. Dash, K. Palaniyandi, S. Ramalingam, S. Sahabudeen, N.S. Raja, Biochim. Biophys. Acta, Biomembr. 1863 (2021) 183490.
[34] S.Y. Kim, D. Khanal, P. Tharkar, B. Kalionis, W. Chrzanowski, Nanoscale Horizons 3 (2018) 430–438.
[35] V. Szentirmai, A. Wacha, C. Németh, D. Kitka, A. Rácz, K. Héberger, J. Mihály, Z. Varga, Anal. Bioanal. Chem. 412 (2020) 4619–4628.
[36] S.K. George, L. Lauková, R. Weiss, V. Semak, B. Fendl, V.U. Weiss, S. Steinberger, G. Allmaier, C. Tripisciano, V. Weber, Int. J. Mol. Sci. 22 (2021) 3839.
[37] F. Perut, G. Graziani, L. Roncuzzi, N. Zini, S. Avnet, N. Baldini, Cells 11 (2022) 778.
[38] E. Nsugbe, H.-L. Ser, H.-F. Ong, L.C. Ming, K.-W. Goh, B.-H. Goh, W.-L. Lee, Diagnostics 12 (2022) 2099.
[39] M.E. Temperini, V. Giliberti, R. Polito, L. Baldassarre, M. Ortolani, OSA Contin 3 (2020) 2564–2572.
[40] K. Rasuleva, S. Elamurugan, A. Bauer, M. Khan, Q. Wen, Z. Li, P. Steen, A. Guo, W. Xia, S. Mathew, ACS Sens. 6 (2021) 4489–4498.
[41] B.Y. Chen, C.W.H. Sung, C. Chen, C.M. Cheng, D.P.C. Lin, C. Te Huang, M.Y. Hsu, Clin. Chim. Acta 493 (2019) 14–19.
[42] M.I. Ramirez, M.G. Amorim, C. Gadelha, I. Milic, J.A. Welsh, V.M. Freitas, M. Nawaz, N. Akbar, Y. Couch, L. Makin, Nanoscale 10 (2018) 881–906.
[43] G. van Niel, D.R.F. Carter, A. Clayton, D.W. Lambert, G. Raposo, P. Vader, Nat. Rev. Mol. Cell Biol. 23 (2022) 369–382.
[44] Y.X.F. Lee, H. Johansson, M.J.A. Wood, S. El Andaloussi, Front. Neurosci. 13 (2019) 1067.
[45] M.E. Temperini, F. Di Giacinto, S. Romanò, R. Di Santo, A. Augello, R. Polito, L. Baldassarre, V. Giliberti, M. Papi, U. Basile, J. Nanobiotechnol. 20 (2022) 1–20.
[46] L. Businaro, O. Limaj, V. Giliberti, M. Ortolani, A. Di Gaspare, G. Grenci, G. Ciasca, A. Gerardino, A. De Ninno, S. Lupi, Microelectron. Eng. 97 (2012).
[47] A. De Ninno, G. Ciasca, A. Gerardino, E. Calandrini, M. Papi, M. De Spirito, A. Nucara, M. Ortolani, L. Businaro, L. Baldassarre, Phys. Chem. Chem. Phys. 17 (2015).
[48] S.D. Gupta, G. Kelp, N. Arju, S. Emelianov, G. Shvets, in: Eur. Conf. Lasers Electro-Optics, Optica Publishing Group, 2017. CH_5_1.
[49] G. Kelp, J. Li, J. Lu, N. DiNapoli, R. Delgado, C. Liu, D. Fan, S. Dutta-Gupta, G. Shvets, Lab Chip 20 (2020) 2136–2153.
[50] P.-T. Shen, S.H. Huang, Z. Huang, J.J. Wilson, G. Shvets, Cells 11 (2022) 1600.
[51] D. Rodrigo, A. Tittl, N. Ait-Bouziad, A. John-Herpin, O. Limaj, C. Kelly, D. Yoo, N. J. Wittenberg, S.-H. Oh, H.A. Lashuel, Nat. Commun. 9 (2018) 1–9.
[52] R. Adato, H. Altug, Nat. Commun. 4 (2013) 1–10.
[53] R. Adato, A.A. Yanik, J.J. Amsden, D.L. Kaplan, F.G. Omenetto, M.K. Hong, S. Erramilli, H. Altug, Proc. Natl. Acad. Sci. USA 106 (2009) 19227–19232.
[54] F. Neubrech, C. Huck, K. Weber, A. Pucci, H. Giessen, Chem. Rev. 117 (2017) 5110–5145.
[55] K. Ratajczak, H. Grel, P. Olejnik, S. Jakiela, M. Stobiecka, Biosens. Bioelectron. (2023) 115644.
[56] J. Wang, X. Wang, X. Zhang, T. Shao, Y. Luo, W. Wang, Y. Han, Front. Oncol. 12 (2022) 884369.
[57] F. Fornari, M. Ferracin, D. Trerè, M. Milazzo, S. Marinelli, M. Galassi, L. Venerandi, D. Pollutri, C. Patrizi, A. Borghi, PLoS One 10 (2015) e0141448.
[58] H. Lang, G.C. Sotiropoulos, M. Dömland, N.R. Frühauf, A. Paul, J. Hüsing, M. Malagó, C.E. Broelsch, J. Br, Surgery (St Louis) 92 (2005) 198–202.
[59] A. Cimino, M. Halushka, P. Illei, X. Wu, S. Sukumar, P. Argani, Breast Cancer Res. Treat. 123 (2010) 701–708.
[60] F. Verdelli, J.J.P.M. Schulpen, A. Baldi, J.G. Rivas, J. Phys. Chem. C 126 (2022) 7143–7151.
[61] D.D. Sjoberg, K. Whiting, M. Curry, J.A. Lavery, J. Larmarange, R J. 13 (2021).
[62] X. Robin, N. Turck, A. Hainard, N. Tiberti, F. Lisacek, J.C. Sanchez, M. Müller, BMC Bioinf 12 (2011) 77.
[63] M.V. Matteo, V. Bove, G. Ciasca, G. Carlino, R. Di Santo, L. Vinti, G. Polidori, V. Pontecorvi, M. Papi, C. Spada, Obes. Surg. 34 (2024) 1496–1504.
[64] M. Nardini, G. Ciasca, A. Lauria, C. Rossi, F. Di Giacinto, S. Romanò, R. Di Santo, M. Papi, V. Palmieri, G. Perini, Front. Aging Neurosci. 14 (2022).
[65] T. Wang, K.W. Anderson, I. V Turko, Anal. Chem. 89 (2017) 11070–11075.
[66] B.W. Sódar, Á. Kittel, K. Pálóczi, K.V. Vukman, X. Osteikoetxea, K. Szabó-Taylor, A. Németh, B. Sperlágh, T. Baranyai, Z. Giricz, Z. Wiener, L. Turiák, L. Drahos, É. Pállinger, K. Vékey, P. Ferdinandy, A. Falus, E.I. Buzás, Sci. Rep. 6 (2016) 1–12.
[67] G. Spizzo, D. Fong, M. Wurm, C. Ensinger, P. Obrist, C. Hofer, G. Mazzoleni, G. Gastl, P. Went, J. Clin. Pathol. 64 (2011) 415–420.
[68] R. Lu, W.-W. Li, A. Katzir, Y. Raichlin, H.-Q. Yu, B. Mizaikoff, Analyst 140 (2015) 765–770.
[69] G. Ciasca, T.E. Sassun, E. Minelli, M. Antonelli, M. Papi, A. Santoro, F. Giangaspero, R. Delfini, M. De Spirito, Nanoscale 8 (2016) 19629–19643.
[70] E. Minelli, G. Ciasca, T.E. Sassun, M. Antonelli, V. Palmieri, M. Papi, G. Maulucci, A. Santoro, F. Giangaspero, R. Delfini, others, Appl. Phys. Lett. 111 (2017) 143701.
[71] H. Wang, Z. Lu, X. Zhao, J. Hematol. Oncol. 12 (2019) 1–21.
[72] U. Basile, L. Miele, C. Napodano, G. Ciasca, F. Gulli, K. Pocino, N. De Matthaeis, A. Liguori, A. De Magistris, G. Marrone, Eur. Rev. Med. Pharmacol. Sci. 24 (2020) 12675–12685.
[73] K. Pocino, C. Napodano, M. Marino, R. Di Santo, L. Miele, N. De Matthaeis, F. Gulli, R. Saporito, G.L. Rapaccini, G. Ciasca, Cancers 14 (2022) 11.
[74] D.R. Dufour, J.A. Lott, F.S. Nolte, D.R. Gretch, R.S. Koff, L.B. Seeff, Clin. Chem. 46 (2000) 2050–2068.
[75] K. Pocino, C. Napodano, L. Gragnani, G. Ciasca, S. Colantuono, S. Marri, L. Vantaggio, F. Gulli, S. Lorini, A. Barini, A. Stefanile, L. Miele, M. Casato, A. L. Zignego, G.L. Rapaccini, M. Marino, M. Visentini, U. Basile, Rheumatology 60 (2021) 4418–4427.
[76] K. Pocino, A. Stefanile, V. Basile, C. Napodano, F. D'Ambrosio, R. Di Santo, C.A. M. Callà, F. Gulli, R. Saporito, G. Ciasca, J. Personalized Med. 13 (2022) 5.
[77] C. Napodano, G. Ciasca, P. Chiusolo, K. Pocino, L. Gragnani, A. Stefanile, F. Gulli, S. Lorini, G. Minnella, F. Fosso, Int. J. Mol. Sci. 24 (2023) 11602.
[78] H.-G. Wan, H. Xu, Y.-M. Gu, H. Wang, W. Xu, M.-H. Zu, Clin. Res. Hepatol. Gastroenterol. 38 (2014) 706–714.
[79] G. Ricco, C. Cosma, G. Bedogni, A. Biasiolo, M. Guarino, P. Pontisso, F. Morisco, F. Oliveri, D. Cavallone, F. Bonino, Cancer Biomarkers (2020) 1–8.
[80] R. Yu, Z. Tan, X. Xiang, Y. Dan, G. Deng, BMC Cancer 17 (2017) 1–10.
[81] M. Tian, Y. Li, W. Liu, L. Jin, X. Jiang, X. Wang, Z. Ding, Y. Peng, J. Zhou, J. Fan, Y. Cao, W. Wang, Y. Shi, Nanoscale 7 (2015) 12988–13010.
[82] W. Sohn, J. Kim, S.H. Kang, S.R. Yang, J.-Y. Cho, H.C. Cho, S.G. Shim, Y.-H. Paik, Exp. Mol. Med. 47 (2015) e184, e184.
[83] G. Szabo, F. Momen-Heravi, Nat. Rev. Gastroenterol. Hepatol. 14 (2017) 455–466.
[84] N. Ludwig, T.L. Whiteside, Expert Opin. Ther. Targets 22 (2018) 409–417.
[85] C. Shao, F. Yang, S. Miao, W. Liu, C. Wang, Y. Shu, H. Shen, Mol. Cancer 17 (2018) 1–8.
[86] R. Kalluri, K.M. McAndrews, Cell 186 (2023) 1610–1626.
[87] D.W. Greening, S.K. Gopal, R.A. Mathias, L. Liu, J. Sheng, H.-J. Zhu, R.J. Simpson, in: Semin. Cell Dev. Biol., Elsevier, 2015, pp. 60–71.
[88] T. Fang, H. Lv, G. Lv, T. Li, C. Wang, Q. Han, L. Yu, B. Su, L. Guo, S. Huang, Nat. Commun. 9 (2018) 1–13.
[89] C.-H. Hsieh, S.-K. Tai, M.-H. Yang, Neoplasia 20 (2018) 775–788.
[90] F. Momen-Heravi, S. Bala, K. Kodys, G. Szabo, Sci. Rep. 5 (2015) 9991.
[91] Y. Wang, C. Zhang, P. Zhang, G. Guo, T. Jiang, X. Zhao, J. Jiang, X. Huang, H. Tong, Y. Tian, Cancer Med. 7 (2018) 1670–1679.
[92] Y. Cho, E. Mezey, J.P. Hardwick, N. Salem Jr., D.L. Clemens, B. Song, Hepatol. Commun. 1 (2017) 675–690.
[93] E. Moratti, M. Vezzalini, L. Tomasello, D. Giavarina, C. Sorio, PLoS One 10 (2015) e0119110.
[94] Y.-E. Cho, E.-J. Im, P.-G. Moon, E. Mezey, B.-J. Song, M.-C. Baek, PLoS One 12 (2017) e0172463.
[95] S.A. Lang, J. Bednarsch, K. Joechle, I. Amygdalos, Z. Czigany, L. Heij, T.F. Ulmer, U.P. Neumann, Expet Rev. Gastroenterol. Hepatol. 15 (2021) 497–510.
[96] D. Povero, H. Yamashita, W. Ren, M.G. Subramanian, R.P. Myers, A. Eguchi, D. A. Simonetto, Z.D. Goodman, S.A. Harrison, A.J. Sanyal, Hepatol. Commun. 4 (2020) 1263–1278.
[97] J. Bissonnette, J. Altamirano, C. Devue, O. Roux, A. Payancé, D. Lebrec, P. Bedossa, D. Valla, F. Durand, H. Ait-Oufella, Hepatology 66 (2017) 555–563.
[98] S. Sukriti, J.S. Maras, C. Bihari, S. Das, A.K. Vyas, S. Sharma, S. Hussain, S. Shasthry, A. Choudhary, M. Premkumar, Aliment, Pharmacol. Ther. 47 (2018) 1151–1161.

[99] C. Peng, Y. Ye, Z. Wang, L. Guan, S. Bao, B. Li, W. Li, Dig. Liver Dis. 51 (2019) 621–631.
[100] Y. Pang, S. Zhang, H. Yang, R.L. Zhou, Beijing Da Xue Xue Bao, Yi Xue Ban= J. Peking Univ. Heal. Sci. 53 (2021) 710–715.
[101] C. Napodano, C. Callà, A. Fiorita, M. Marino, E. Taddei, T. Di Cesare, G.C. Passali, R. Di Santo, A. Stefanile, M. Fantoni, J. Personalized Med. 11 (2021) 385.
[102] S.Y. Kim, D. Khanal, B. Kalionis, W. Chrzanowski, Nat. Protoc. 14 (2019) 576–593.
[103] T. Ito, S. Okazaki, Nature 406 (2000) 1027–1031.
[104] A. John-Herpin, A. Tittl, L. Kühner, F. Richter, S.H. Huang, G. Shvets, S. Oh, H. Altug, Adv. Mater. (2022) 2110163.
[105] P. Auricchio, M. Finotti, Transplantology 4 (2023) 71–84.
[106] C.F. Subasi, U.E. Aykut, Y. Yilmaz, Eur. J. Gastroenterol. Hepatol. 27 (2015) 137–141.
[107] H. Shin, B.H. Choi, O. Shim, J. Kim, Y. Park, S.K. Cho, H.K. Kim, Y. Choi, Nat. Commun. 14 (2023) 1644.